

Transition Metal Dichalcogenide Metaphotonics and Self-coupled Polariton Platform Realized by CVD Bottom-up Method

fuhuan sheng

CUHK

yaoqiang zhou

cuhk

zhenhe zhang

soochow University

Jingwen Ma

The Chinese University of Hong Kong

Huanjun Chen

Guangdong Province Key Laboratory of Display Material and Technology, Sun Yat-sen University

<https://orcid.org/0000-0003-4699-009X>

Shaojun Wang

Eindhoven University of Technology

Zhefeng Chen (✉ zfchen86@suda.edu.cn)

School of Optoelectronic Science and Engineering & Collaborative Innovation Center of Suzhou Nano Science and Technology, Soochow University, Suzhou 215006, China

Jian-Bin Xu

Chinese University of Hong Kong

Article

Keywords:

Posted Date: February 15th, 2022

DOI: <https://doi.org/10.21203/rs.3.rs-1335516/v1>

License:   This work is licensed under a Creative Commons Attribution 4.0 International License.

[Read Full License](#)

Version of Record: A version of this preprint was published at Nature Communications on September 23rd, 2022. See the published version at <https://doi.org/10.1038/s41467-022-33088-0>.

Transition Metal Dichalcogenide Metaphotonics and Self-coupled

Polariton Platform Realized by CVD Bottom-up Method

Fuhuan Shen¹, Yaoqiang Zhou¹, Zhenhe Zhang², Jingwen Ma¹, Huanjun Chen³,
Shaojun Wang², Zefeng Chen^{2,1,*}, Jianbin Xu^{1,*}

1. Department of Electronic Engineering, The Chinese University of Hong Kong, Shatin, N.T., Hong Kong SAR, P. R. China.

2. School of Optoelectronic Science and Engineering and Collaborative Innovation Center of Suzhou Nano Science and Technology, Soochow University, Suzhou 215006, China

3. State Key Lab of Optoelectronic Materials and Technologies, Guangdong Province Key Laboratory of Display Material and Technology, School of Electronics and Information Technology, Sun Yat-sen University, Guangzhou 510275, P. R. China

* Corresponding Authors. Email: zfchen86@suda.edu.cn (Z. F. Chen) and jbxu@ee.cuhk.edu.hk (J. B. Xu).

Abstract

The exotic electronic and optical properties of the transition metal dichalcogenides(TMDCs) opens up new opportunities in the field of dielectric metaphotonics. Although some interesting photonic phenomena have been demonstrated in nanostructures fabricated from mechanical exfoliated TMDCs, it is still challenging to realize the large scale TMDCs metaphotonics structure with controllable geometric parameters. Here, we experimentally demonstrate the MoS₂ metaphotonics structures through the CVD bottom-up method, which support both the dielectric resonant modes and self-coupled polaritons. To be specific, we realize the magnetic-type surface lattice resonance(M-SLR) in the 1D MoS₂ metaphotonics structure with extremely low material loss. As a proof of concept, we further exhibit a self-coupled exciton-SLR polariton via the spatial dispersion with abnormal coupling strength to the mode volume and the Rabi splitting up to 170meV. Bright Mie modes and self-coupled anapole-exciton polaritons with unambiguous anti-crossing behavior are also realized in 2D MoS₂ metaphotonics structures. We argue that the TMDCs structure based on this CVD bottom-up fabrication method not only can realize nanoresonator but also can be extended to other metaphotonic structure such as metasurface, metalens and slab photonic crystal.

1 Introduction

2 The rapid progress of the metaphotonics have boost the development of an abundance
3 of fields including the optics nonlinearity, luminescence enhancement and far-field
4 manipulation[1][2][3][4][5][6], thereby opening up the possibilities in the applications
5 such as single-photon switch, nano-scale laser and metasurface [3][7][8][9].
6 Comparing to the plasmonic counterpart, the dielectric nanostructure is predicted to
7 exhibit the similar strong field confinement at subwavelength while the dissipative
8 losses are greatly reduced[10], enabling both the realization of strong response of the
9 electric and magnetic modes[11][12]. Recent studies in the dielectric metaphotonics
10 have successfully achieved some novel physical phenomena such as the dielectric
11 quasi-BIC mode and supercavity[13][14][15], making the dielectric structure a superior
12 platform in the fields of quantum optics and condensed-matter[16][17]. Moreover, the
13 dielectric-based 2D metaphotonics structures also show great potential in wavefront
14 engineering with ultrathin profiles, boosting the development of the optics devices for
15 the practical applications, such as metasurfaces, metaholograms, and
16 metalenses[18][19].

17 For these dielectric metaphotonic structures from Mie scatter to metasurface, even
18 to waveguiding, one of great demand is high-index dielectric materials, which can
19 reduce the geometric scale of the device and improve the quality factor of
20 resonator[20][21]. So far, most of metaphotonic structures are fabricated from
21 conventional semiconductor (e.g. Silicon with refraction index of 3.7-3.9 in visible and
22 near infrared range) and oxide semiconductor (e.g. TiO₂ with refraction index of 2.5-
23 2.7 in visible and near infrared range) through top-down etching process[22][23].

24 Recent works have confirmed that transitional metal dichalcogenides(TMDCs) is
25 a great promising material for dielectric metaphotonics structure[11][24]. Comparing
26 to traditional semiconductors such as Si, TMDCs not only show a higher refractive
27 index($n=4\sim 5$), but also exhibit distinct excitonic responses covering from the visible to
28 the infrared range, leading to multiple interesting physical phenomena and
29 applications[20][21][25][26]. For example, distinct Mie resonances and hybrid

1 anapole-exciton states have been demonstrated in the nanodisks fabricated from
2 exfoliated multilayer WS₂[11]. However, achieving a large scale TMDC metaphotonics
3 structure with great geometry control has not been realized in the experiment yet. In the
4 previous works, TMDCs nanopattern is fabricated through top-down process where the
5 exfoliated TMDC flakes are dry etched with the nano etching mask on the
6 top[11][24][27]. As a result, the dimension of metaphotonics structure will be limited
7 by the size of exfoliated TMDCs flake, and the height is not controllable
8 either[24][28][28]. Moreover, this etching method is hard to yield nanostructures with
9 vertical sidewalls for nano column or nano disk for some materials such as MoS₂[12].

10 Here, we propose a bottom-up CVD fabrication method to realize the concept of
11 TMDCs metaphotonics, which are demonstrated to support the multiple dielectric
12 resonant modes and the self-coupled polaritons. The TMDC metaphotonics structure is
13 fabricated from transitional metal nanopattern followed by CVD sulfidation process to
14 convert the Mo pattern to MoS₂ pattern. With this method, we successfully fabricate
15 the millimeter-area MoS₂ meta-structures with uniform geometric parameters(such as
16 periods, height and diameters). The magnetic-type surface lattice resonance(M-SLR)
17 with extremely low material loss is for the first time demonstrated in the 1D MoS₂
18 metaphotonics structures, as well as the hybrid polaritons formed by the M-SLR self-
19 coupled to the excitons of MoS₂ with Rabi splitting up to 170meV. Moreover, anapole-
20 exciton polariton with unambiguous anti-crossing dispersion is realized in the 2D MoS₂
21 meta-structures. We argue that this CVD bottom-up method paves the path to realize
22 TMDCs-based metaphotonic structure, such as nanoresonator and metasurface.

23

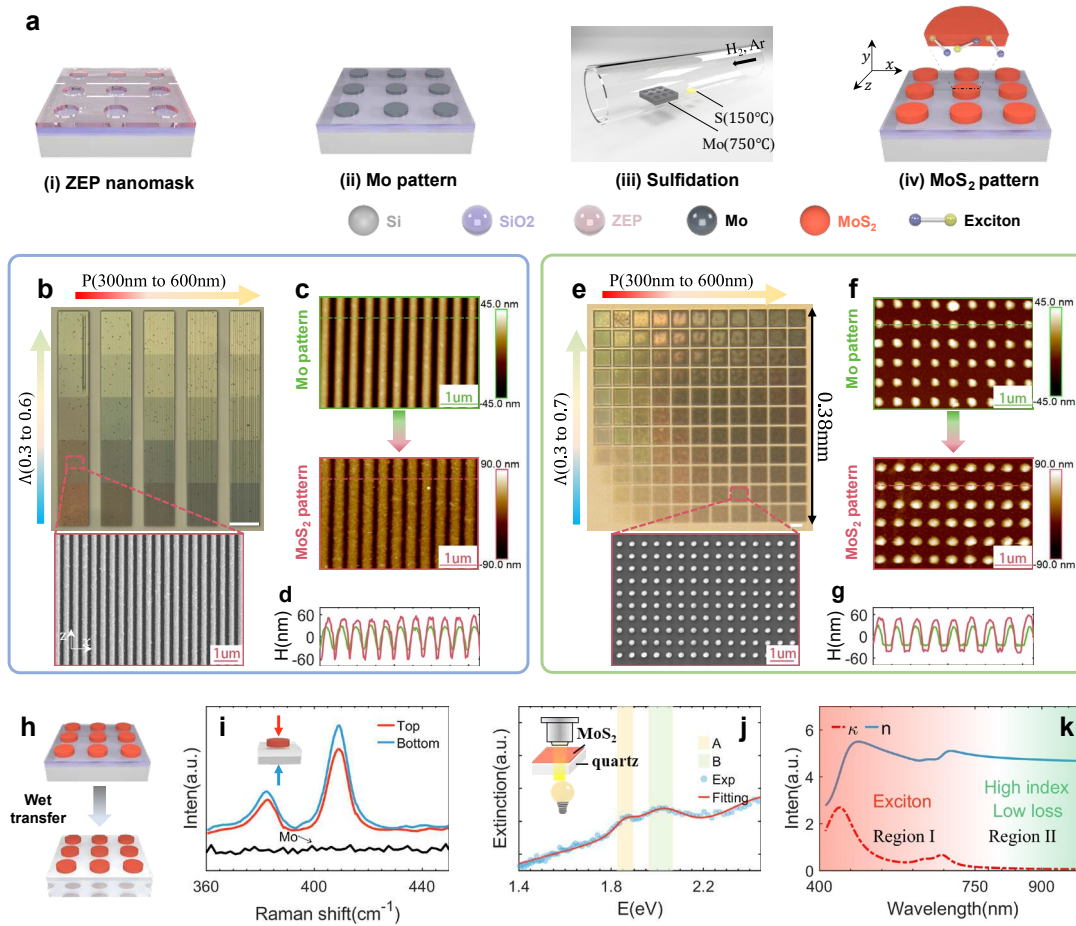


Fig.1 | Fabrication procedure and morphology & material properties of MoS₂ metaphotonic structures. **a)** Schematic figure to outline the CVD bottom-up fabrication process, which starts from Mo nano pattern (i-ii) and follows by sulfidation process to convert the Mo pattern to MoS₂ pattern (iii-iv). **b)** Microscope figures of 1D MoS₂ meta-structures with various period (P) and filling factor (Λ) where scale bar is $20\mu\text{m}$. Below is the SEM figure. **c)** AFM figures for 1D Mo pattern (before sulfidation) and MoS₂ patterns (after sulfidation). **d)** Height profile of the Mo pattern (green) and MoS₂ pattern (red) as indicated by the dashed lines in **c**. **e-g)** Same as **b-d** but for the 2D MoS₂ meta-structures. **h)** Schematic figure of transferring the MoS₂ metastructures from SiO₂($2\mu\text{m}$)/Si substrate to transparent quartz substrate. **i)** Raman spectra from both top (red) and bottom (blue) sides of the MoS₂ structures. Black curve is the Raman spectrum for Mo pattern. **j)** Extinction spectrum (blue circles) of the MoS₂ film and the corresponding fitting curve (red curve). Yellow and green areas indicate the positions of A and B excitons. Inset is the schematic setup. **k)** The real (blue solid curve) and imaginary (red dashed curve) refractive index of MoS₂ based on the Lorentz model (See eq(S28)). The red area and green area roughly separate the excitonic response (Region I) and high refractive index & low loss (Region II) regions of the MoS₂.

19

20 Figure 1a outlines the procedure to fabricate the MoS₂ metastructures (here we use disk
 21 array as an example). Firstly, using standard electron-beam lithography (EBL)

1 technology and E-beam evaporation, we fabricate Mo nanopattern on SiO₂/Si substrate.
2 Then the patterned Mo structure is sent to the quartz-tube furnace for sulfidation process
3 with the temperature of 750°C. The Mo pattern would be chemically converted to the
4 MoS₂ pattern after sulfidation process.

5
6 Figure 1b shows the microscope image of the 1D MoS₂ metastructures after sulfidation.
7 The color of the corresponding structure evolves with different period P and filling
8 factor $\Lambda = w/P$ where w is the width of original Mo pattern(see the detailed
9 definition of geometric parameters of 1D MoS₂ metastructures in SI part 2.1). The
10 period and geometric shape exhibit excellent uniformity in the scanning electron
11 microscopy(SEM) image on the bottom. The comparison of SEM images of Mo pattern
12 and corresponding MoS₂ pattern in Figure S3 indicates that the period remains
13 unchanged during the sulfidation process while the lateral geometry of the constituent
14 component(i.e., grating bar) is extended in the in-plane direction. The atomic force
15 microscope(AFM) images of Mo pattern and corresponding MoS₂ in Figure 1c
16 confirms the unaltered period and the lateral extension, but also shows the extension in
17 the out-of-plane direction(height) due to the sulfidation process. The height
18 profiles(indicated by the dashed lines in Figure 1c) can be clearly seen in the Figure 1d
19 where the height of original Mo pattern is increased from $55 \pm 5\text{nm}$ (green curve) to
20 $110 \pm 10\text{nm}$ (red curve) when converted to MoS₂ pattern. Figure 2e-g shows the similar
21 results in the 2D MoS₂ metastructures whose lateral size is up to 0.38mm(Figure 2e).
22 Distinct to the top-down(etch) method based on the exfoliated TMDCs[11][12][24], our
23 method shows the controllable geometric properties of the metastructures. The
24 dimension of MoS₂ metastructure is only limited to the electron-beam lithography
25 pattern and the height of MoS₂ can be controlled through the evaporation thickness of
26 Mo pattern[29].

27
28 To characterize the material and optical properties of the MoS₂ metastructures we
29 transfer the patterned MoS₂ from SiO₂(2 μm)/Si substrate to transparent quartz substrate

1 via the wet transfer method(Figure 1h)[30]. The Raman spectra is firstly measured from
2 both top and bottom sides to confirm the chemical conversion due to the sulfidation
3 process. Comparing with the Mo pattern(before sulfidation, black curve), two
4 characteristic peaks($E_{2g}^1 \approx 382\text{cm}^{-1}$ and $A_g \approx 409\text{cm}^{-1}$) are emerged for the both sides
5 of MoS₂ pattern which indicate that the sulfidation procedure for the patterned Mo
6 structures is completed[31]. Then the extinction spectrum(blue circles in Figure 1j) of
7 the MoS₂ film is obtained through transmission measurements(inset in Figure 1j). By
8 applying the transfer matrix method(SI part 2.3) we fit the extinction spectrum in Figure
9 1j(red curve) where the dielectric function($\varepsilon = \varepsilon' + i\varepsilon''$) of MoS₂ is described by the
10 Lorentz model with both responses of A, B and C excitons considered. Then the
11 refractive index and extinction coefficient $n + i\kappa = \sqrt{\varepsilon' + i\varepsilon''}$ is calculated. As is
12 shown in Figure 1k, within the range of 400nm-750nm(Region I), both n and κ
13 exhibits the strong dispersion due to the excitonic responses. While in the Region
14 II(>750nm), the refractive index $n \approx 4.7$ and shows negligible dispersion with
15 wavelength. Meanwhile, in this region the corresponding material loss(κ) is close to
16 zero, indicating great potential in the design and fabrication of the high quality optics
17 nanodevices. We also notice that, distinct to the strong anisotropic properties of
18 dielectric function of exfoliated TMDCs, previous works indicate that the MoS₂
19 metastructures fabricated via sulfidation process show the reduced anisotropic due to
20 the various orientation of MoS₂ layers[31][29][32]. Consequently, in the following, the
21 isotropic dielectric function of MoS₂ is applied in the simulations. The excellent match
22 between experiment and simulation results confirms the isotropic dielectric properties
23 of the MoS₂ metastructures from an optics point of view.

24

25 A1-A3(see the definition in SI part 2.1) are selected as the representative examples of
26 1D MoS₂ metastructures. As the SEM figures in Figure 2a show, the period is fixed at
27 400nm and width of the grating bar is increased from A1-A3. Figure 2b shows the
28 extinction spectra measured under p polarization(see results under s polarization in SI
29 part 2.6). In addition to the A&B excitonic responses observed in the Figure 1j, a surface

1 lattice resonant(SLR) mode appears on the red side of the A exciton due to the coupling
2 of individual grating bar to the Rayleigh anomalies(RAs) where the diffraction wave
3 becomes evanescent at the interface of two media(see SI part 1.2). The experimental
4 extinction spectra can be well reproduced by the simulation(top part of the Figure 2a).
5 The calculated near field distributions of the resonant mode(inset figures in Figure 2a)
6 indicate the magnetic nature of the mode where the electric field circulates inside of the
7 structure and magnetic field is along the z-direction[33], and we label this resonance as
8 M-SLR(i.e., magnetic-type SLR. See electric-type SLR in SI part 2.6). The linewidth
9 of M-SLR is estimated as $\gamma \approx 100\text{meV}(A1)$ by the Lorentz fitting(purple dashed-lines
10 in the Figure 2a)[34]. The origin of linewidth of the spectra is basically from two parts:
11 1) the intrinsic material loss, 2) the radiation loss[35]. To separate the influence of the
12 radiation loss, in Figure 2c we calculate the extinction spectra for the same 1D
13 structures(inset in the Figure 2c) where the refractive index $n=4.7$ (to match the
14 refractive index of MoS₂ shown in the Figure 1k) and extinction coefficient κ varies
15 from 0(no material loss) to 0.2. The period is set as 400nm and width of the grating bar
16 is chosen as 110nm in the simulation, rendering the resonant energy of M-SLR
17 approaching 1.7eV(i.e., A1). The resonant frequency is mainly dependent on n and
18 therefore no unambiguous resonant frequency shift is observed with κ . Through
19 fitting(black dashed curves in Figure 2c), we abstract the linewidths of the
20 corresponding M-SLR in Figure 2c. As Figure 2d figure indicates, the linewidths(γ)
21 show the near-linear relation(dashed curve) with κ . At zero material loss($\kappa=0$), the
22 linewidth is around 96meV which is purely ascribed to the radiation loss. By inserting
23 our experiment result into the fitting curve in Figure 2c(yellow star), we find that the
24 M-SLR(A1) in Figure 2b show near-zero material loss where the extinction coefficient
25 is estimated as $\kappa < 10^{-2}$. Extinction spectra for other 1D metastructures can be seen in
26 Figure S6.

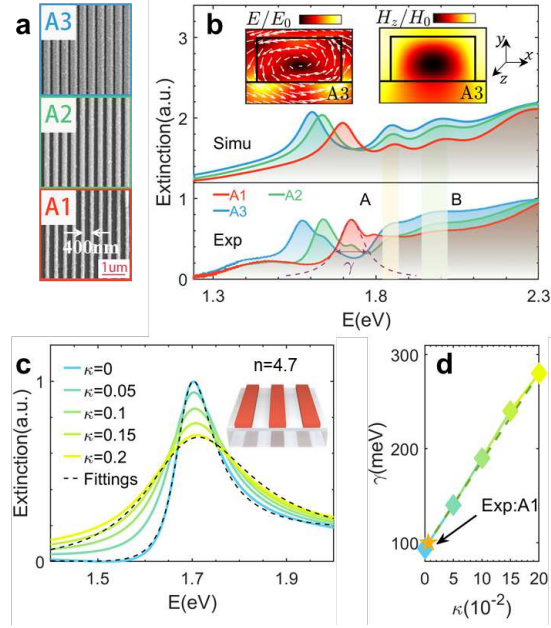


Fig.2 | Optical properties of the 1D MoS₂ meta-structures. **a)** SEM figures for A1- A3. **b)** Experimental and simulated extinction spectra for various 1D MoS₂ meta-structures(A1-A3) under normal incidence. Insets are the near field distributions of the electric field and magnetic field(H_z) of the resonant mode. White arrows in electric field distribution are the projections of real part of the electric field in the x-y plane. **c)** Simulated extinction spectra for the 1D dielectric meta-structures with extinction coefficient κ from 0 to 0.2. Black dashed curves are the fitting curves for $\kappa = 0$ and $\kappa = 0.2$. To avoid mess other fitting curves are not shown. Inset is the schematic setup in the simulation. **d)** The corresponding linewidths abstracted from the fitting results of the extinction spectra in **c**. In simulation, the structures are all in the homogeneous dielectric environment whose refractive index is 1.46.

The spatial dispersion of the A1-A3(Figure 3a) is obtained through the angle-resolved transmission measurements. Figure 3b shows the corresponding simulation results which will reproduce the experiment ones. A triple-coupled model(SI part 1.1, parameters are in the Table S1) is applied to describe the dispersion of three branches observed in the Figure 3a,b which is given by

$$(\omega_{cav} - \omega)(\omega - \omega_A)(\omega - \omega_B) + g_A^2(\omega - \omega_B) + g_B^2(\omega - \omega_A) = 0 \quad (1.)$$

where ω_{cav} , ω_A and ω_B represent the resonant frequencies of cavity mode, A exciton and B exciton; g_A and g_B represent the coupling strengths of A and B exciton to the cavity. Within this model, totally three polariton dispersions(i.e., lower, middle and upper polaritons) are generated due to the coupling between the M-SLR

1 demonstrated in Figure 2b and A&B excitons from MoS₂. As indicated by the green(lp,
 2 i.e., lower polariton), blue(mp, i.e., middle polariton) and red(up, i.e., upper polariton)
 3 curves, a clear anti-crossing behavior is visible in the dispersion spectra, especially for
 4 the lower polariton and middle polariton. While for the upper polariton, the dispersion
 5 is negligible, possibly due to the weaker oscillator strength of B exciton and the large
 6 energy detuning to the resonant mode. Without losing the generality, we will focus on
 7 the coupling between A exciton and resonant modes in the latter part.

8
 9 To give an unambiguous illustration of dispersion behaviour observed in the Figure 3a-
 10 b, we apply the simulation by artificially modifying the dielectric function of material
 11 constituting the metastructures. The designed structure is the same as Figure 2b while
 12 the dielectric function of the material is described by the Lorentz model:

$$13 \quad \varepsilon = \varepsilon_0 + f \frac{\omega_0^2}{\omega_0^2 - \omega^2 - i\gamma\omega} \quad (2.)$$

14 where $\varepsilon_0=16$ is the background permittivity; $\omega_0 = 2.1\text{eV}$ and $\gamma = 40\text{meV}$ are the
 15 resonant frequency and linewidth of the exciton; f is the corresponding oscillator
 16 strength[11]. We consider three sets of the dielectric function(Figure 3(c)): (i) $f=0$ (i.e.,
 17 no excitonic response); (ii) $f=0.2$; (iii) $f=0.4$. As Figure 3d shows, when no excitonic
 18 response is considered in the system(i), the M-SLR shows the linear dispersion curves,
 19 associated with the $(\pm 1, 0)$ diffraction orders(blue dashed-dot curves), i.e., RAs(see
 20 SI part 1.2). Such linear dispersions due to RAs are also observed in the
 21 experiment(Figure S6a-d) where the M-SLR are far detuning from the A&B excitonic
 22 resonance.

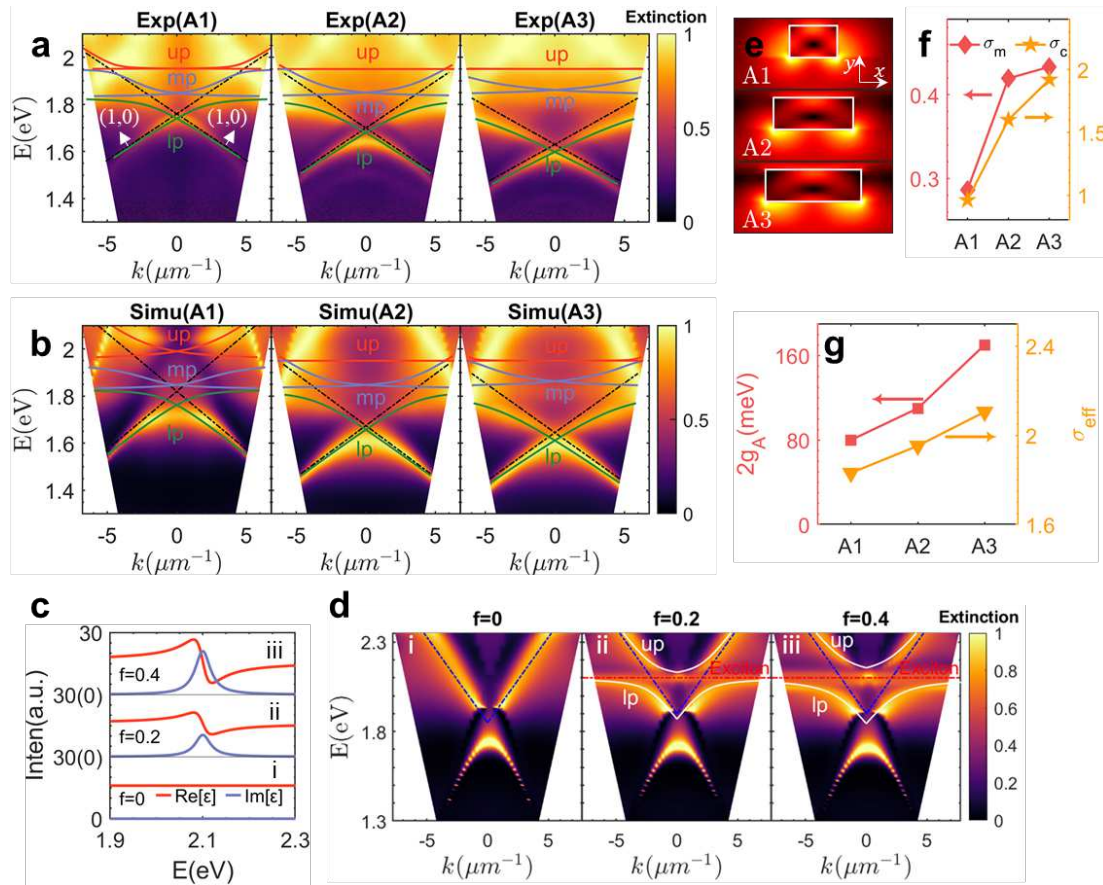
23
 24 However, once the exciton is coupling in the system(ii and iii in Figure 3d), the linear-
 25 dispersed M-SLR(bule dashed-dot curves) would strongly interact with the exciton(red
 26 dashed-dot curves) where two polaritons states(lp: lower polariton; up: upper polariton)
 27 are generated with a clear anti-crossing behaviour. By fitting results with the polariton
 28 dispersion(white curves), the Rabi splitting can be calculated as 170meV(ii) and

1 240meV(ii) which meets the previous reported $\Omega \propto \sqrt{f}$ relation[34]. Above analyses
 2 confirm the self-coupled mechanism shown in the Figure 3a-b where the cavity
 3 modes(M-SLR) strongly interact with the internal excitons, resulting in the robust and
 4 highly dispersive polariton behaviour. In previous studies where the 2D TMDCs is
 5 externally coupled to the dielectric resonant structure[36][37], no unambiguous
 6 polariton behavior is observed due to the low efficiency of the spatial overlap of the
 7 exciton and external field of resonant mode. In contrast, in this study, through the self-
 8 coupled mechanism the exciton is strongly interaction with the internal field(insets of
 9 the Figure 2a) of the mode, resulting in the incredible enhancement of the coupling
 10 strength.

11

12 Meanwhile, we surprisingly observed that from A1-A3 the coupling strength g_A is
 13 increased from 40meV(A1) to 85meV(A3). The previous studies on strong coupling of
 14 the TMDCs plasmonic resonance system indicated that to achieve larger Rabi splitting
 15 the mode volume need to be “shrunk” so as to obtain stronger light-matter
 16 interaction[38]. However, in our system the condition is distinct as the metastructure
 17 itself is composed of the TMDCs. Though the increase of the mode volume would
 18 degrade the interaction strength between single exciton and confined field, the benefit
 19 comes with more excitons entering in the coupling. To provide quantitative analyses,
 20 we do the theoretical calculation and simulation to shows the origin of the abnormal
 21 increase of the coupling strength with the mode volume. As indicated by eq(S10-S11),
 22 Rabi splitting $\Omega \propto \frac{\sqrt{N}}{\sqrt{V}}$ where N is the number of excitons entering the coupling and V
 23 is the mode volume[1]. In this context, we define mode area $\sigma_m = \iint \frac{\epsilon E^2 ds}{\max[\epsilon E^2]}$ and
 24 cross section area $\sigma_c = w_{grating} \times h_{grating}$ (the cross section area for MoS₂
 25 metastructures). One thus could calculate the mode volume $V = \sigma_m \times z$ and exciton
 26 number $N \propto (\sigma_c \times z)$. As such, the Rabi splitting can be deduced as $\Omega \propto \frac{\sqrt{\sigma_c}}{\sqrt{\sigma_m}}$ (defined
 27 as $\sigma_{eff} = \frac{\sqrt{\sigma_c}}{\sqrt{\sigma_m}}$). Figure 3e exhibits the electric field distribution of cross sections of

1 A1-A3 from the simulation results(Figure 2d) where the width of 1D structure increases.
 2 As Figure 3f shows, both σ_c and σ_m are calculated and increased from A1 to A3. The
 3 increase of σ_c indicates that more excitons enter in the coupling(thus increase the
 4 coupling strength) while the increase of σ_m reflects the increase of the mode volume
 5 of resonant mode which would reduce the coupling intensity. The combined effect is
 6 reflected by the effective area σ_{eff} . Figure 3g compares σ_{eff} with the Rabi
 7 splitting(represented by $2g_A$) and both shows the same increasing tendency from A1-
 8 A3. Consequently, though the increase of width of grating would increase mode volume
 9 of the PC, more excitons would be introduced in the coupling process during this
 10 process, resulting in the increase of total coupling strength of the system.



12 **Fig.3 | Spatial dispersion of self-coupled polaritons in the 1D MoS₂ PC.** **a)** The
 13 spatial dispersion of 1D MoS₂ PC for A1-A3. The black dashed-dot curves are
 14 dispersions of the cavity modes(magnetic modes) of the PC, corresponding to the (0,
 15 ± 1) refraction orders(noticed by the white arrows). Green, blue and red solid curves
 16 represent the lower, middle and upper polaritons respectively. **b)** The simulated spatial
 17 dispersion of 1D MoS₂ PC for A1-A3. **c)** The real part(red) and imaginary(blue) parts
 18 of the dielectric functions calculated by the Lorentz model with $f=0$ (i), $f=0.2$ (ii) and
 19 $f=0.4$ (iii). **d)** The spatial dispersion of the 1D dielectric meta-structures with dielectric

1 function corresponding to **c**. The geometric parameters for **d**: height=100nm,
2 width=200nm, period=400nm. **e**) The electrical distribution of the cross section of 1D
3 MoS₂ PC(x-y plane) for A1-A3. The MoS₂ region are marked by the white box within
4 the figure. **f**) Mode area σ_m and cross section area σ_c for A1-A3 and the unit is
5 10^4nm^2 . **g**) Coupling strength of A exciton to the cavity mode($2g_A$) and effective area
6 σ_{eff} for A1-A3.

7
8 To introduce more possible optical dielectric modes, a 2D MoS₂ metastructure(square
9 disk array) is designed and fabricated(Figure 1e and Figure 4a). As Figure 4a shows,
10 we choose samples with period $P=510\text{nm}$ and filling factor $\Lambda = d/P$ (d is the
11 diameter of the single disk) varies from 0.3 to 0.48, i.e., H1-H7 as the representative
12 examples(see definition in SI part 2.1). The extinction spectra are shown in Figure 4b
13 and can be well reproduced by the simulation in Figure 4c. Multiple optical modes,
14 including electric dipole(ED), magnetic dipole(MD) and anapole, appear in various
15 frequency ranges. To be specific, we here select H3(white dashed curve in Figure 4c)
16 as an example. As Figure 4e shows, the mode residing within the range of 1.25eV to
17 1.75eV can be decomposed into two bright Mie modes: ED(orange curve) and MD(blue
18 curve) modes. In Figure 4e, ED mode exhibits the distorted electric field distribution
19 which is like placing two charges of equal quantity but opposite signs at two ends of
20 the disk. In contrast to it, MD shows the circulating electric field, similar to the field
21 distribution of the inset figure in the Figure 2b. In Figure 4c, the ED and MD modes
22 are firstly separated in the frequency domain at small Λ (0.3 to 0.33) and gradually
23 overlap with Λ (0.36-0.48) due to the different geometric parameter dependence
24 properties of ED and MD modes of the dielectric array[39]. These two modes exhibit
25 strong scattering intensity at resonance which corresponds to the characteristics of the
26 bright mode. Another mode(marked by the green triangle in Figure 4d) near the B
27 excitonic resonance exhibits the characteristics of anapole mode. Figure 4e shows the
28 near field distribution of anapole mode where the toroidal dipole and electric dipole
29 modes simultaneous exist[11]. Due to the destructive interference of these two modes
30 at far field, the scattering of the anapole would be greatly deduced(dark mode)[40].

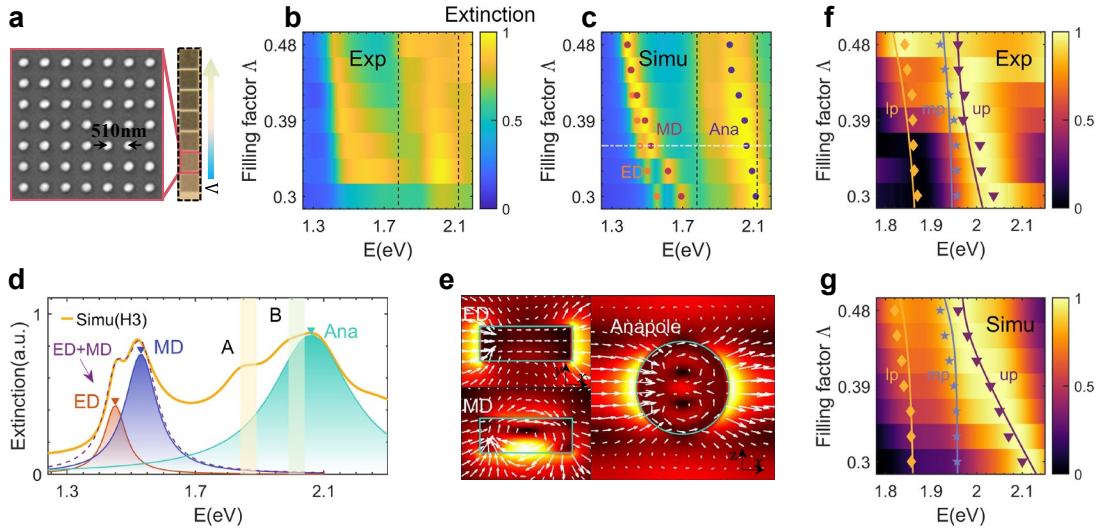


Fig.4 | Light-matter interaction of the exciton and Mie modes in the 2D MoS₂ PC.

a) The optical figure of the 2D MoS₂ PC. The inset red box shows the SEM figure of corresponding region. The scale bar is 30 μ m. **b-c)** The extinction spectra map for H1-H7 (marked within the black dashed box in **a**) from the experiment measurements (**b**) and simulation (**c**). **d)** The simulated spectra for H3 (white dashed line in **c**). ED, MD, anapole, A exciton, B exciton as well as the RA are marked in the figure. **e)** The electrical field distributions of the corresponding ED, MD and anapole modes in **d**. **f-g)** Zoomed-in extinction spectra abstracted from the black dashed boxes in **b** and **c**. The yellow diamonds, blue stars and purple triangles represent the lower, middle and upper polaritons from the experiment (**f**) and simulation (**g**) results. The corresponding solid curves are calculated by eq(1) and coupling strengths $g_A \approx 55meV$ and $g_B \approx 20meV$.

At last, we demonstrate the enhanced light-matter interaction in the anapole modes of the 2D MoS₂ metastructures. As Figure 4b and 4c show, the anapole mode of the MoS₂ disk array shows a red shift with the Λ and the coupling of A and B exciton can be realized. Figure 4f,g shows the zoomed-in spectra of the Figure 4b,c (black dashed-box) separately. The spatial dispersions of triple polaritons are again shown in the Figure 4f,g where a clear anti-crossing behaviour is demonstrated in the lower (yellow curves) and upper polariton (purple curves) due to the coupling of A exciton to the anapole. While for B exciton, the weaker oscillator strength hinders the obvious observation of the anti-crossing phenomenon in the middle polariton (blue curve).

To sum up, we present a CVD bottom-up method to design and fabricate the

1 metaphotonics structures based on the high-index TMDCs where the dielectric resonant
2 modes and their interactions to exciton are investigated in the visible and near-infrared
3 range. The magnetic-type surface lattice mode with low material loss is firstly
4 demonstrated in the 1D MoS₂ metaphotonics structure. In such a compact platform the
5 strong self-coupling is achieved with Rabi-splitting over 170meV. We further observed
6 the abnormal increase of the coupling strength with the mode volume and a quantitative
7 explanation is given with the theoretical analyses and simulation. Last but not the least,
8 multiple Mie-type modes including ED, MD and anapole modes as well as anapole-
9 exciton polariton are realized in the 2D MoS₂ metaphotonics structure. Our method
10 could be easily extended to other TMDCs material such as WS₂ and MoTe₂ to fully
11 utilize their distinct excitonic responses and phase transition properties. The strategy in
12 this work paves a new road to design and fabricate the dielectric nano photonic
13 structures for the fields of the nonlinear optics and the quantum light to take great
14 advantage of the high refractive index and unique excitonic response of the TMDCs.

18 **Acknowledgements**

19 The work is in part supported by Research Grants Council of Hong Kong, particularly,
20 via Grant Nos. AoE/P-02/12, AoE/P-701/20, 14203018, N_CUHK438/18, and CUHK
21 Group Research Scheme, CUHK Postdoctoral Fellowship, and ITS/390/18 by
22 Innovation and Technology Commission, Hong Kong SAR Government.

23 **References**

- 24 [1] R. Chikkaraddy *et al.*, “Single-molecule strong coupling at room temperature
25 in plasmonic nanocavities,” *Nature*, vol. 535, no. 7610, p. 127, 2016.
- 26 [2] B. Munkhbat, A. Canales, B. Küçüköz, D. G. Baranov, and T. O. Shegai,
27 “Tunable self-assembled Casimir microcavities and polaritons,” *Nature*, vol.
28 597, no. 7875, pp. 214–219, 2021.
- 29 [3] C. Schneider *et al.*, “An electrically pumped polariton laser,” *Nature*, vol. 497,
30 no. 7449, pp. 348–352, 2013.
- 31 [4] Z. Wang *et al.*, “Giant photoluminescence enhancement in tungsten-
32 diselenide–gold plasmonic hybrid structures,” *Nat. Commun.*, vol. 7, p. 11283,
33 2016.
- 34 [5] A. F. Cihan, A. G. Curto, S. Raza, P. G. Kik, and M. L. Brongersma, “Silicon
35 Mie resonators for highly directional light emission from monolayer MoS₂,”

- 1 *Nat. Photonics*, vol. 12, no. 5, pp. 284–290, 2018.
- 2 [6] R. Bose, D. Sridharan, H. Kim, G. S. Solomon, and E. Waks, “Low-photon-
3 number optical switching with a single quantum dot coupled to a photonic
4 crystal cavity,” *Phys. Rev. Lett.*, vol. 108, no. 22, pp. 1–5, 2012.
- 5 [7] J. Cuadra, D. G. Baranov, M. Wersäll, R. Verre, T. J. Antosiewicz, and T.
6 Shegai, “Observation of Tunable Charged Exciton Polaritons in Hybrid
7 Monolayer WS₂-Plasmonic Nanoantenna System,” *Nano Lett.*, vol. 18, no. 3,
8 pp. 1777–1785, 2018.
- 9 [8] N. Liu *et al.*, “Plasmonic analogue of electromagnetically induced transparency
10 at the Drude damping limit,” *Nat. Mater.*, vol. 8, no. 9, pp. 758–762, 2009.
- 11 [9] N. Liu, M. Mesch, T. Weiss, M. Hentschel, and H. Giessen, “Infrared perfect
12 absorber and its application as plasmonic sensor,” *Nano Lett.*, vol. 10, no. 7,
13 pp. 2342–2348, 2010.
- 14 [10] T. Liu, R. Xu, P. Yu, Z. Wang, and J. Takahara, “Multipole and multimode
15 engineering in Mie resonance-based metastructures,” *Nanophotonics*, vol. 9,
16 no. 5, pp. 1115–1137, 2020.
- 17 [11] R. Verre, D. G. Baranov, B. Munkhbat, J. Cuadra, M. Käll, and T. Shegai,
18 “Transition metal dichalcogenide nanodisks as high-index dielectric Mie
19 nanoresonators,” *Nat. Nanotechnol.*, vol. 14, no. July, pp. 679–684, 2019.
- 20 [12] T. D. Green, D. G. Baranov, B. Munkhbat, R. Verre, T. Shegai, and M. Käll,
21 “Optical material anisotropy in high-index transition metal dichalcogenide Mie
22 nanoresonators,” *Optica*, vol. 7, no. 6, p. 680, 2020.
- 23 [13] Z. Liu *et al.*, “High- Q Quasibound States in the Continuum for Nonlinear
24 Metasurfaces,” *Phys. Rev. Lett.*, vol. 123, no. 25, pp. 1–6, 2019.
- 25 [14] K. Koshelev, S. Lepeshov, M. Liu, A. Bogdanov, and Y. Kivshar,
26 “Asymmetric Metasurfaces with High- Q Resonances Governed by Bound
27 States in the Continuum,” *Phys. Rev. Lett.*, vol. 121, no. 19, p. 193903, 2018.
- 28 [15] M. V. Rybin *et al.*, “High- Q Supercavity Modes in Subwavelength Dielectric
29 Resonators,” *Phys. Rev. Lett.*, vol. 119, no. 24, pp. 1–5, 2017.
- 30 [16] K. Koshelev *et al.*, “Subwavelength dielectric resonators for nonlinear
31 nanophotonics,” *Science (80-.)*, vol. 367, no. 6475, pp. 288–292, 2020.
- 32 [17] A. S. Solntsev, G. S. Agarwal, and Y. Y. Kivshar, “Metasurfaces for quantum
33 photonics,” *Nat. Photonics*, vol. 15, no. 5, pp. 327–336, 2021.
- 34 [18] L. Jin *et al.*, “Dielectric multi-momentum meta-transformer in the visible,” *Nat.*
35 *Commun.*, vol. 10, no. 1, 2019.
- 36 [19] E. Arbabi, A. Arbabi, S. M. Kamali, Y. Horie, M. S. Faraji-Dana, and A.
37 Faraon, “MEMS-tunable dielectric metasurface lens,” *Nat. Commun.*, vol. 9,
38 no. 1, 2018.
- 39 [20] A. I. Kuznetsov, A. E. Miroshnichenko, M. L. Brongersma, Y. S. Kivshar, and
40 B. Luk’yanchuk, “Optically resonant dielectric nanostructures,” *Science*
41 *(80-.)*, vol. 354, no. 6314, 2016.
- 42 [21] L. Sortino *et al.*, “Bright single photon emitters with enhanced quantum
43 efficiency in a two-dimensional semiconductor coupled with dielectric nano-
44 antennas,” *Nat. Commun.*, vol. 12, no. 1, pp. 1–9, 2021.

- 1 [22] K. Tanaka *et al.*, “Chiral bilayer all-dielectric metasurfaces,” *ACS Nano*, vol.
2 14, no. 11, pp. 15926–15935, 2020.
- 3 [23] A. Y. Zhu *et al.*, “Giant intrinsic chiro-optical activity in planar dielectric
4 nanostructures,” *Light Sci. Appl.*, vol. 7, no. 2, p. 17158, 2018.
- 5 [24] X. Zhang *et al.*, “Azimuthally Polarized and Unidirectional Excitonic Emission
6 from Deep Subwavelength Transition Metal Dichalcogenide Annular
7 Heterostructures,” *ACS Photonics*, 2021.
- 8 [25] M. M. Ugeda *et al.*, “Giant bandgap renormalization and excitonic effects in a
9 monolayer transition metal dichalcogenide semiconductor,” *Nat. Mater.*, vol.
10 13, no. 12, pp. 1091–1095, 2014.
- 11 [26] K. D. Park, T. Jiang, G. Clark, X. Xu, and M. B. Raschke, “Radiative control
12 of dark excitons at room temperature by nano-optical antenna-tip Purcell
13 effect,” *Nat. Nanotechnol.*, vol. 13, no. 1, pp. 59–64, 2018.
- 14 [27] M. Nauman *et al.*, “Tunable unidirectional nonlinear emission from transition-
15 metal-dichalcogenide metasurfaces,” *Nat. Commun.*, vol. 12, no. 1, pp. 1–11,
16 2021.
- 17 [28] H. Zhang *et al.*, “Hybrid exciton-plasmon-polaritons in van der Waals
18 semiconductor gratings,” *Nat. Commun.*, vol. 11, no. 1, pp. 1–9, 2020.
- 19 [29] S. Jang, S. J. Kim, H. J. Koh, D. H. Jang, S. Y. Cho, and H. T. Jung, “Highly
20 Periodic Metal Dichalcogenide Nanostructures with Complex Shapes, High
21 Resolution, and High Aspect Ratios,” *Adv. Funct. Mater.*, vol. 27, no. 46, pp.
22 1–8, 2017.
- 23 [30] X. Wang, K. Kang, K. Godin, S. Fu, S. Chen, and E.-H. Yang, “Effects of
24 solvents and polymer on photoluminescence of transferred WS₂ monolayers,”
25 *J. Vac. Sci. Technol. B*, vol. 37, no. 5, p. 052902, 2019.
- 26 [31] C. Yim *et al.*, “Investigation of the optical properties of MoS₂ thin films using
27 spectroscopic ellipsometry,” *Appl. Phys. Lett.*, vol. 104, no. 10, 2014.
- 28 [32] J. Henzie, J. E. Barton, C. L. Stender, and T. W. Odom, “Large-area nanoscale
29 patterning: Chemistry meets fabrication,” *Acc. Chem. Res.*, vol. 39, no. 4, pp.
30 249–257, 2006.
- 31 [33] G. W. Castellanos, P. Bai, and J. Gómez Rivas, “Lattice resonances in
32 dielectric metasurfaces,” *J. Appl. Phys.*, vol. 125, no. 21, 2019.
- 33 [34] F. Shen *et al.*, “Investigation on the Fano-Type Asymmetry in Atomic
34 Semiconductor Coupled to the Plasmonic Lattice,” *ACS Photonics*, vol. 8, no.
35 12, pp. 3583–3590, 2021.
- 36 [35] F. Wang and Y. R. Shen, “General properties of local plasmons in metal
37 nanostructures,” *Phys. Rev. Lett.*, vol. 97, no. 20, pp. 1–4, 2006.
- 38 [36] H. Wang *et al.*, “Resonance Coupling in Heterostructures Composed of Silicon
39 Nanosphere and Monolayer WS₂: A Magnetic-Dipole-Mediated Energy
40 Transfer Process,” *ACS Nano*, vol. 13, no. 2, pp. 1739–1750, 2019.
- 41 [37] S. Lepeshov *et al.*, “Tunable Resonance Coupling in Single Si Nanoparticle-
42 Monolayer WS₂ Structures,” *ACS Appl. Mater. Interfaces*, vol. 10, no. 19, pp.
43 16690–16697, 2018.
- 44 [38] J. Wen *et al.*, “Room-temperature Strong Light-Matter Interaction with Active

- 1 Control in Single Plasmonic Nanorod Coupled with Two-Dimensional Atomic
2 Crystals,” *Nano Lett.*, vol. 17, no. 8, pp. 4689–4697, 2017.
- 3 [39] J. Jang, T. Badloe, Y. Yang, T. Lee, J. Mun, and J. Rho, “Spectral Modulation
4 through the Hybridization of Mie-Scatterers and Quasi-Guided Mode
5 Resonances: Realizing Full and Gradients of Structural Color,” *ACS Nano*,
6 2020.
- 7 [40] A. E. Miroshnichenko *et al.*, “Nonradiating anapole modes in dielectric
8 nanoparticles,” *Nat. Commun.*, vol. 6, pp. 1–8, 2015.
- 9

Supplementary Files

This is a list of supplementary files associated with this preprint. Click to download.

- [Supportinginformation.docx](#)